# Nanoimprinted Quasi-2D Perovskites Toward High-Performance Polarization-Sensitive Photodetectors

*Duanzijing Liu[#1], Qi Wei[#1], Lyuchao Zhuang[1], Ming Liu[2], Longhui Zeng[3], Hui Ren[1], Mingjie Li[1], Shu Ping Lau*[1]*

[1]Department of Applied Physics, Photonic Research Institute, The Hong Kong Polytechnic University, Hung Hom, Kowloon, Hong Kong, P. R. China

E-mail: apsplau@polyu.edu.hk

[2]Department of Materials Science and Engineering, City University of Hong Kong, Kowloon, Hong Kong, P. R. China

[3]Department of Electrical and Computer Engineering, University of California San Diego, La Jolla, California 92093, United States

Keywords: 2D perovskites, phase distribution, polarization-sensitive photodetector

**Abstract:** The demand for high-performance polarization-sensitive perovskite photodetectors (PSPPDs) has driven research to develop new materials that enable efficient light harvesting and polarization detection. Herein, we report a PSPPD based on nanoimprinted quasi-two-dimensional (quasi-2D) halide perovskite thin films with vertical gradient phase distribution. The nanoimprinting method was utilized to create nanoscale linear patterns on the surface of the film. It enables polarized light detection and enhances absorption. According to the results of transient absorption analysis, we confirmed a vertical gradient phase distribution along the longitudinal direction of quasi-2D perovskite $(PEA)_2(MA)_{n-1}Pb_nI_{3n+1}$ ($PEA^+$ = $C_6H_5CH_2CH_2NH_3^+$, $MA^+$ =

$CH_3NH_3^+$, $n$ = 3), which facilitates efficient carrier transfer and separation, leading to improved device performance. Our PSPPDs demonstrate outstanding photo-response with a large responsivity of approximately 90 A/W and a high detectivity reaching the order of $10^{12}$ Jones. The photoluminescence of the quasi-2D perovskite film exhibits an anisotropy ratio of 2.05, and the PSPPD reaches a polarization sensitivity of 1.68. Our findings offer insight into the feasibility of developing perovskite materials for PSPPDs, which have potential applications in imaging, sensing, and communication technologies.

## 1. Introduction

Polarization-sensitive photodetectors (PDs) are attracting much attention for their ability to detect the direction and degree of polarization of light, which is valuable in bio-signal detection,[1] astronomy,[2] display technology,[3] and military applications.[4] In recent years, halide perovskites have found promising applications in polarization-sensitive photodetection due to their excellent optoelectronic properties, such as high absorption coefficient,[5] long carrier diffusion length[6], and tunable band gap.[7-10] In general, the polarization-sensitive perovskite photodetectors (PSPPDs) can be made by using perovskites with intrinsically anisotropic crystal structures or by combining perovskites with other materials that have anisotropic crystal structures into heterojunctions;[11-14] or by forming perovskites with anisotropic morphology, especially nanowires (NWs).[15-17]

Despite these achievements, preparing large-scale and high-quality perovskite crystals with an anisotropic crystal structure is challenging and time-consuming. The fabrication of perovskite NWs is compliant with complex techniques like capillary force-assisted growth,[15-16] space-confined growth,[17] and oriented force growth.[18-19] Moreover, the optoelectronic performances of PSPPDs are not competitive compared with non-polarized perovskite PDs.[20] Attempts were made to prepare PSPPDs with thin films to achieve higher performance. Through the nanoimprinting method, Zhan and coworkers demonstrated a linear-grating structure on $MAPbI_3$ ($MA^+ = CH_3NH_3^+$) film to realize polarization detection.[21] With the aid of porous photonic crystals, the perovskite PD exhibited a responsivity of 12.67 A/W under white light. Song and coworkers designed moiré-lattices PDs with dual nanograting based on $MAPbI_3$ films.[22] The dual nanograting structure enhanced the PD's light harvesting while achieving polarization detection, and the responsivity was improved up to 15.62 A/W.

Quasi-2D perovskites are a class of perovskite materials that have a layered crystal structure of alternating organic cation layers and an inorganic perovskite layer, unlike traditional 3D perovskites that have a three-dimensional network of corner-sharing octahedra. The layered structure of quasi-2D perovskites provides several advantages, such as outstanding structural stability,[23-24] controllable phase distribution[25], and tunable bandgaps.[26] The interlayer charge transfer mechanism of quasi-2D perovskites can also enhance carrier diffusion and help mitigate charge trapping and recombination

processes, leading to improved charge transport properties.[27-28]

We believe there is enormous scope for improving the performance of PSPPD by exploiting the advantages of quasi-2D halide perovskites. Herein, we report a PSPPD based on quasi-2D perovskite film. The thin film of $(PEA)_2MA_2Pb_3I_{10}$ ($PEA^+$ = $C_6H_5CH_2CH_2NH_3^+$) prepared by the hot casting method demonstrates a gradient phase distribution, in which quasi-2D and three-dimensional (3D) phases separate vertically. Nanoimprinting is employed to introduce a linear pattern on the film's surface. The linear pattern has two functions here. First, the anisotropic structure enables the device to respond to the light polarization. This is because dielectric contrast exists between the material and the surroundings. Due to this dielectric contrast, the absorption intensity is different when the electric field of the light is perpendicular and parallel to the linear material structure.[29] Second, the grating structure traps light in channels between perovskite arrays so the film can absorb more light instead of being reflected in the surroundings.[21, 30] Therefore, the light harvesting of the film can be enhanced. The PSPPD prepared via such a facile and scalable process has advantages in the following two aspects. i) Compared with PSPPD based on NWs and single crystals, the device in this work is prepared through spin-coating followed by a nanoimprinting process performed concurrently with annealing, which is more convenient to operate. ii) The phases' spatial separation promotes charge carrier extraction from quasi-2D phases to 3D phases, which highly prolongs carrier lifetime and improves the

performance of PSPPD. The device presents a high responsivity of 89.8 A/W and a detectivity of $1.58\times10^{12}$ Jones under 0.22 μW/cm$^2$ 633 nm illumination. Meanwhile, polarization detection is available across a broadband range, and the maximum anisotropy ratio of photocurrent and photoluminescence reaches 1.68 and 2.05, respectively, under 532 nm illumination.

## 2. Results and Discussion

The preparation process of the target sample and a schematic of the anticipated film structure are shown in **Figure 1a**. With the hot-casting process followed by an imprinting operation, our perovskite film was expected to possess a vertical gradient 2D/3D phase distribution with the linear nanopattern on the surface (we abbreviated the target film as L-G-PVK film hereinafter). The hot-casting temperature and the imprinting pressure were discreetly controlled to ensure the pattern of the DVD inner layer was accurately replicated onto the film, while the gradient-phase-distribution-structure produced by hot casting was not damaged. The method to control imprinting pressure and the suitable pressure value are described in detail in the experimental section. To evaluate the optical properties and optoelectronic performance of L-G-PVK film, we also prepared three other samples for comparison as presented in Figure 1b: a control sample with neither linear pattern nor vertical gradient structure (C-PVK) prepared by the standard spin-coating method, a film with a linear pattern, but without vertical gradient structure (L-PVK) prepared by the standard spin-coating method with

a subsequent nanoimprinting method during annealing process; a film with vertical gradient structure but without a linear pattern (G-PVK) prepared by the hot-casting method without nanoimprinting during annealing process.

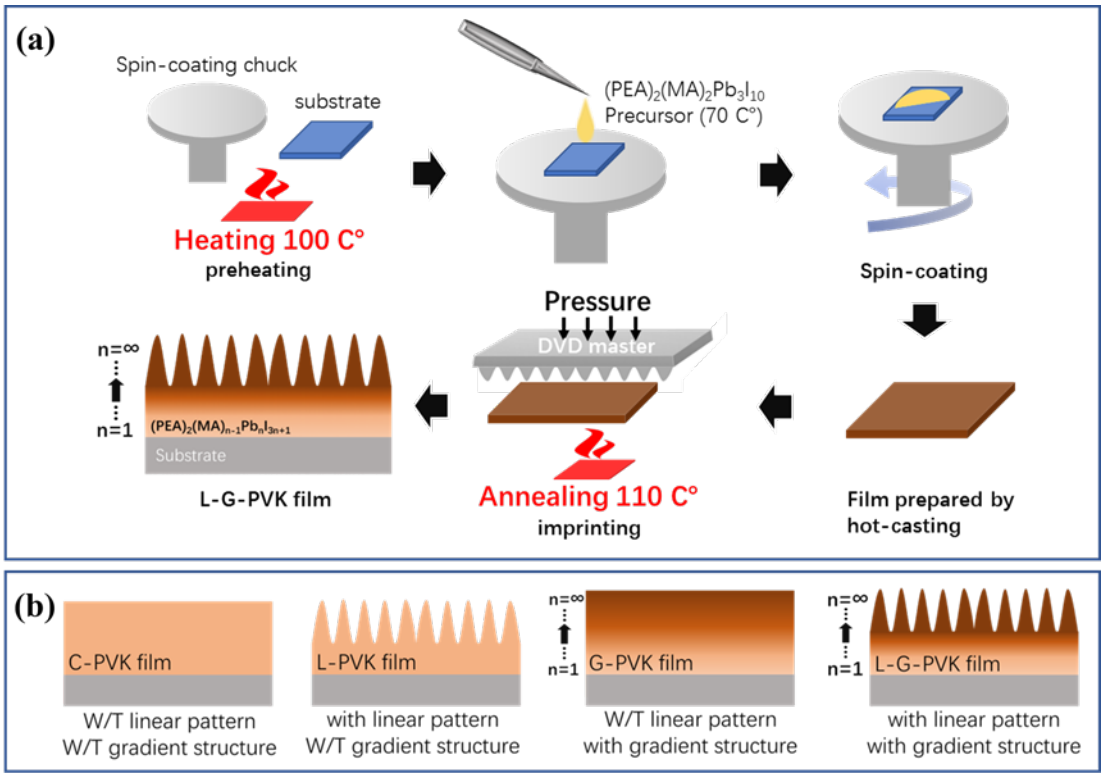


**Figure 1.** a) Schematic illustration of the preparation method of linear-gradient perovskite (L-G-PVK) film. b) Schematic illustrations of C-PVK film, L-PVK film, G-PVK film, and L-G-PVK film.

**Figures 2a** and 2b present photographs of the L-G-PVK film prepared on a silicon substrate from two different shooting angles. In Figure 2a, the clear visibility of the substrate indicates the film is semitransparent, and the imprinted area in the red dotted box is less transparent than the surrounding area, showing that the imprinted film gets better light absorption ability than the unimprinted area. The colorful reflection observed from another shooting angle in Figure 2b is a typical diffraction phenomenon

caused by a linear grating structure [30-31], just like what we see on the back of a DVD plate. It implies the formation of a linear pattern on the film surface. To further demonstrate that we obtained the linear nanopattern on the film, we used an atomic force microscope (AFM) to measure the film surface morphology. As shown in the AFM height image (Figure 2c), it is proved that the regular and clear linear nanopattern was formed. Figure 2d presents a height profile extracted from the location of the red arrow in Figure 2c. The linear grating with around 0.7 μm in period and approximately 70 nm in height can be observed. This structure matches well with the design of the DVD inner layer (Figure S1). Those results collectively prove that the DVD's linear nanograting structure is successfully copied onto the film surface.

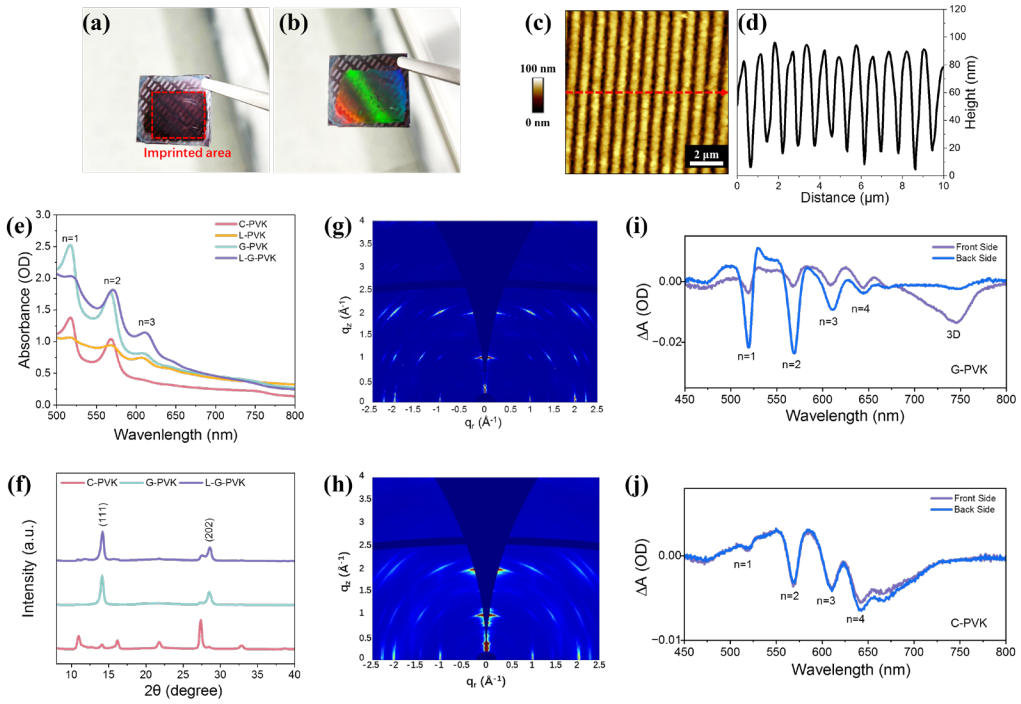


**Figure 2.** a,b) Photographs of L-G-PVK film on the silicon substrate from different shooting angles. c) AFM height image of L-G-PVK film surface and d) the height profile corresponding to the red arrow. e) Absorbance spectra and f) XRD patterns of

PVK films. GIWAXS pattern of g) G-PVK film and h) C-PVK film. TA spectra collected under the front and back sides photoexcitation of i) G-PVK and j) C-PVK film at 100 ps.

The absorbance spectra of the four films above are shown in Figure 2e. All the films exhibit multiphase absorption peaks. The peaks at 517 nm, 569 nm, 610 nm, and 750 nm correspond to the perovskite phase of $n$ = 1, 2, 3, and 3D phases, respectively.[32] From 525 nm to longer bands, the L-PVK film obtains a higher absorbance than the C-PVK film, and the L-G-PVK film generally brings a higher absorbance than the G-PVK film, which can be attributed to the enhanced light harvesting resulting from the linear pattern structure. X-ray diffraction (XRD) was employed to characterize the crystal structure of as-synthesized perovskite films, as shown in Figure 2f. L-G-PVK and G-PVK film present two significant diffraction peaks at 14.2° and 28.6° corresponding to (111) and (202) crystal planes of quasi-2D phases or (110) and (220) planes of 3D-like phases.[23] However, in C-PVK film, diffraction peaks of the 3D-like phase are less identifiable than those of L-G-PVK and G-PVK. The higher relative intensities of diffraction peaks at 14.2° and 28.6° in L-G-PVK film and G-PVK film reflect than that in C-PVK film can be attributed to higher 3D-like phase contents or better orientation of quasi-2D phases caused by hot-casting. To better understand the crystal orientation in films under hot-casting preparation, grazing-incidence wide-angle X-ray scattering (GIWAXS) was employed to characterize the crystal structure of G-PVK film (Figure 2g) and C-PVK film (Figure 2h). With a grazing-incident angle of 0.1°, the G-PVK film

exhibits sharper diffraction points than the C-PVK film, demonstrating that hot casting enhances crystal orientation. Besides, in the out-of-plane direction, the C-PVK film reveals a diffraction pattern corresponding to (0k0) planes of small-*n* phases, while those diffraction points do not appear in the G-PVK film. This is because, in G-PVK film, quasi-2D phases tend to adopt a vertical orientation.[32-33] The as-confirmed crystal orientation in G-PVK film is desirable because it benefits charge carrier transportation,[33] which is an important issue for PDs.

The hot-casting process can produce a vertical gradient phase distribution, where PVK phases distribute in an order that aligns from low-n value to high-n value from the bottom to the top of the film.[23, 34] Although there is no consensus on the specific mechanism of this phenomenon, it was speculated to be related to the local molar ratio changing of precursors during the rapid evaporation of the solvent.[35] The transient absorption (TA) measurements were conducted to examine whether the film's perovskite phases distribute following the vertical gradient phase distribution. A 400 nm femtosecond laser was used to excite the front and back sides (the glass substrate side) of the PVK films, and the induced absorption changes (ΔA) as functions of both probe wavelength and time were recorded. Figure 2i shows the TA spectra at the indicated delay times of the G-PVK film, in which several ground-state bleach (GSB) peaks are observed, which can be assigned to $n$ = 1, 2, 3, 4, and 3D-like phases. The TA spectrum under the front-excitation (0.63 μJ $cm^{-2}$) is dominated by the bleach signals

corresponding to 3D phases at 745 nm, whereas the bleach peaks corresponding to quasi-2D phases located in lower bands are weak.

In contrast, the spectrum under the back-excitation exhibits strong bleach signals corresponding to $n$ = 1, 2, 3, and 4 perovskite phases but no prominent signal of the 3D phase. For comparison, no noticeable difference occurred between the front and back side excited spectra in the C-PVK film (Figure 2j). The difference in the TA spectra between back-side and front-side excitations implies that the small-$n$ phases are mainly located at the bottom of the G-PVK film, and large-$n$ phases are primarily located at the top. To further confirm the phase distribution originated from the hot casting, photoluminescence (PL) spectra (with 532 nm exciting laser) of L-G-PVK film were measured from both the front side and the back side (Figure S2). The PL intensity corresponding to quasi-2D phases is higher under the back side excitation, while this phenomenon is absent in the C-PVK film (Figure S2b). PL and TA measurements proved that the vertical quasi-2D/3D gradient structure was formed via hot casting.

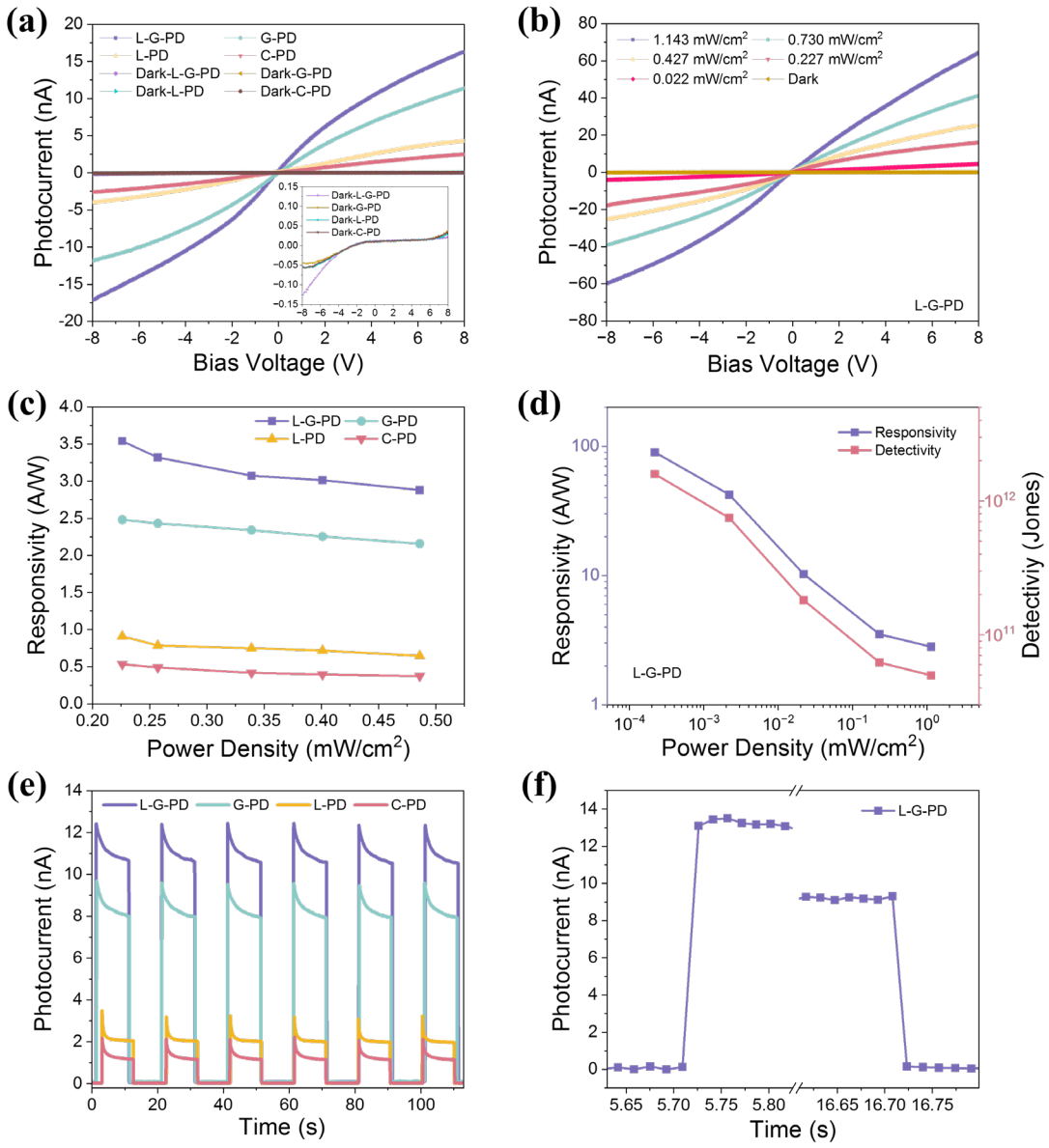


**Figure 3.** Photoelectric measurements of perovskite photodetectors. a) *I-V* curves of C-PD, L-PD, G-PD, and L-G-PD under 0.227 mW/cm$^2$ 633 nm illumination. The dark current curves are magnified inside the picture. b) *I-V* curves of L-G-PD under different light intensities of 633 nm illumination. c) R of C-PD, L-PD, G-PD, and L-G-PD under different light intensities of 633 nm illumination. d) R and D* of L-G-PD under 633 nm illumination with different light intensities. e) *I-t* curves of C-PD, L-PD, G-PD, and L-G-PD under 0.227 mW/cm$^2$ 633 nm illumination with 5 V bias. f) Response speed curve of L-G-PD.

We measured the optoelectronic performances of PDs based on L-G-PVK, L-PVK, G-PVK, and C-PVK (named L-G-PD, L-PD, G-PD, and C-PD, respectively). Cr/Au electrodes were deposited on $Si/SiO_2$ substrates and patterned by photolithography. Then, perovskite films were prepared on the substrates. **Figure 3a** shows the current–voltage (IV) curves of L-G-PD, L-PD, G-PD, and C-PD at 8 V bias in dark and under light illumination (633 nm, 0.227 $mW/cm^2$). The curves exhibit the linear relationship between photocurrents and voltages, demonstrating a good Ohmic contact between perovskite films and Au electrodes. The photocurrent of L-PD (4.27 nA) is around 1.6 times greater than that of C-PD (2.56 nA), which is attributed to the optical absorption enhancement. The photocurrent of G-PD (11.39 nA) is over 4.4 times higher than that of C-PD, indicating the effective spatial separation of photoexcited electron-hole pairs in the vertical heterojunction structure. The photocurrent of L-G-PD (16.27 nA) is over 6.3 times higher than that of C-PD, which originates from the double enhancement of the grating structure on the film surface and vertical gradient phase distribution. Another important parameter of PDs obtained from Figure 3a is light on/off ratios, which is the ratio of photocurrent and dark current (abbreviated as $I_p$ and $I_d$ here) of the PD. The magnified view of the dark current of the four samples is shown at the bottom of Figure 3a. With 8 V bias voltage, the light on/off ratio of L-G-PD, G-PD, L-PD and C-PD are calculated to be $7.67\times10^2$ ($I_p$= 16.27 nA, $I_d$=21.2 pA), $3.25\times10^2$ ($I_p$= 11.39 nA, $I_d$=35.1 pA), $1.50\times10^2$ ($I_p$= 4.27 nA, $I_d$=28.4 pA) and $0.79\times10^2$ ($I_p$=2.56 nA, $I_d$=32.4 pA), respectively. In Figure 3b, *I–V* curves of L-G-PD under illumination (633 nm) with

power density from 0.022 to 1.143 mW/cm$^2$ with a bias voltage of 8 V show that the photocurrent rises with increasing light power. Figure 3c presents the responsivity (R), given by[22, 36]

$$R = \frac{(I_{ph} - I_{dark})}{PS} \quad (1)$$

where $P$ is the light intensity, and $S$ is the effective area, of L-G-PD, G-PD, L-PD, and C-PD under the illumination with $P$ changing from 0.226 to 0.486 mW/cm$^2$ (corresponding *I-V* curves of G-PD, L-PD, and C-PD are shown in Figure S3). $R$ of C-PD, L-PD, G-PD, and L-G-PD increase sequentially under the same light intensity, and for every single PD, the $R$ decreases as the light intensity increases, corresponding to the photoconductive device behavior features. Detectivity ($D^*$) is determined by[22]

$$D^* = \frac{R\sqrt{S}}{\sqrt{2eId}} \quad (2)$$

where $R$ is responsivity, $S$ is the effective area, $e$ is the elementary charge, and $I_d$ is the dark current). $D^*$ is another key parameter of a PD that reflects the ability to detect light with weak intensity. D* of C-PD, L-PD, G-PD, and L-G-PD were calculated and exhibited in Figure S4 and revealed the same trend as R. We further measured the light-intensity-dependent performance of L-G-PD with the light intensity changing from 1.14 mW/cm$^2$ to 0.22 μW/cm$^2$, as shown in Figure 3d. Corresponding photocurrents under weak light intensities are shown in Figure S5. It was found that $R$ reaches the highest value (89.8 A/W) under the light intensity of 0.22 μW/cm$^2$. It is shown that $D^*$ presents the same trend as $R$ and reaches the highest value of $1.58\times10^{12}$ Jones at 0.22 μW/cm$^2$. The temporal current of the light switch by the current-time (I–t) curves shown in

Figure 3e prove that C-PD, L-PD, G-PD, and L-G-PD are stable with repeated light on-off cycles. Figure 3f presents the response time of L-G-PD (Response curves of C-PD, L-PD, and G-PD are also shown in Figure S6). The rise ($\tau_r$) and decay ($\tau_d$) time of the device are defined as the time taken for the current increase from 10% to 90% of steady-state photocurrent and vice versa. It is shown that $\tau_r$ and $\tau_d$ of L-G-PD are measured to be 17 ms and 15 ms (due to the limitation of the test instrument, shorter time intervals cannot be captured), respectively. The noise current of C-PD, L-PD, G-PD, and L-G-PD were measured under 4 V bias with no illumination, as shown in Figure S7, and we obtained noise spectral densities of each device by Fast Fourier Transform (FFT) from corresponding dark current noises.[23, 37] Dark current noise from level per unit bands (1 Hz) for C-PD, L-PD, G-PD, and L-G-PD are measured to be $2.07\times10^{-2}$, $2.30\times10^{-2}$, $8.89\times10^{-2}$ and $8.26\times10^{-2}$ pA/Hz$^{1/2}$, respectively. Dark current noises of G-PD and L-G-PD are higher than C-PD and L-PD, but the values are still in the same order of magnitude. Photocurrents of L-G-PD under different power densities of 375 nm, 447 nm, 532 nm, 633 nm, and 750 nm lights were tested (Figure s8a-S8e), and corresponding responsivity as a function of power density for wavelengths are shown in Figure S8f. It can be seen that L-G-PD exhibits broadband photo-response, and in the tested light intensity range, L-G-PD presents the highest responsivity to 633 nm light. There is a controversial point that requires analysis: insulating ligands in quasi-2D perovskites hinder interlayer charge transport, thereby impedes device performance. Then, does the higher content of $MAPbI_3$ or the vertical gradient structure causes higher

responsivity of G-PD than C-PD? To clarify this concern, we prepared PDs of $MAPbI_3$ with the same device structure as C-PD. Figure S9a presents *I-V* curves of $MAPbI_3$ under several light intensities, and Figure S9b presents *R* at 8 V calculated from the *I-V* curves. The responsivity of PDs made of pure $MAPbI_3$ is still lower than G-PD. So, it can be proved that the higher responsivity of L-G-PD and G-PD than L-PD and C-PD is mainly caused by the gradient structure rather than the higher $MAPbI_3$ content.

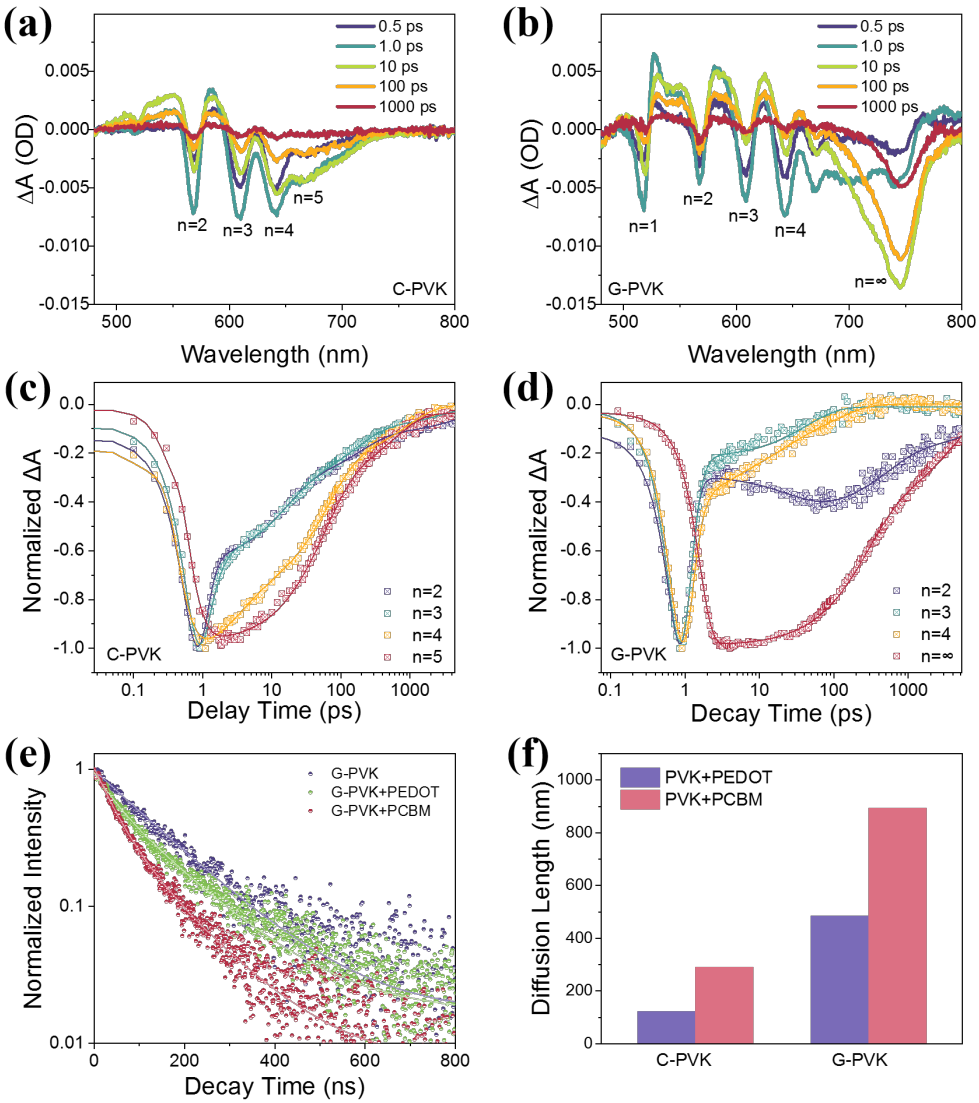


**Figure 4.** TA spectra at various delay times of the a) C-PVK and b) G-PVK film and corresponding kinetics profiles probed at different wavelengths of c) C-PVK and d)

G-PVK film under front-excitation. e) TRPL spectra at the emission center for the G-PVK, G-PVK/PEDOT, and G-PVK/PCBM thin films. f) Electron/hole diffusion length of G-PVK film and C-PVK film. Carrier diffusion lengths were estimated according to a 1D carrier diffusion model.

To gain insights into the photo-physics of perovskite thin films, the charge carrier dynamics in quasi-2D perovskite films were further studied by TA spectroscopy. TA spectra at selected delay times of C-PVK film and G-PVK film are presented in **Figures 4a** and 4b, respectively. The control perovskite C-PVK film features three pronounced ground-state bleach (GSB) peaks at 567, 609, and 644 nm corresponding to $n = 2$, 3, and 4 phases in the TA spectra. In stark contrast to C-PVK perovskite, TA spectra of G-PVK depict a distinct photobleaching (PB) peak of 3D-like phases at 746 nm with intensity growing until ~10 ps. TA kinetics profiles from G-PVK film and C-PVK film probed at the corresponding peak positions are shown in Figures 4c and 4d, respectively. The short decay component for the control film exhibits time constants of 0.29 ps ($n = 2$) and 0.28 ps ($n = 3$) (Table S1), which is closely matched with the formation time constant of 0.44 ps for GSB at 668 nm. Note that the bleaching signal at $n = 2$ and $n = 3$ have additional slow decay components with a long lifetime, suggesting that carriers accumulate in the $n = 2$ and 3 phases, resulting from the incomplete charge transfer between the different phases. Moreover, the GSB peak at 640 nm ($n = 4$) demonstrates non-obvious charge transfer to the high-energy phase, but only recombination occurs. In contrast, the decay kinetics for $n \leq 5$ phases of G-PVK perovskite are dominated by

the fast decay component and in good agreement with the rapid formation time of 3D-like phases, according to the fitting parameters (Table S2). In the G-PVK perovskite film, the fast decay time for the $n$ = 2, $n$ = 3, $n$ = 4, and $n$ = 5 phases is determined to be 0.21, 0.33 ps, 0.33 and 0.59, respectively (Fig. 4d), while the buildup time of 0.91 ps for the 3D-like phase. These results demonstrate that charge carrier transfer (most likely the electrons in our case) occurs inside the reconstructed phases, enabling more efficient energy transfer from small-$n$ phases to large-$n$ phases.[28] Photogenerated electrons are mainly assembled in 3D-like phases on top of the G-PVK film, and the carriers have a specific spatial distribution. In this case, those trapped carriers can produce an additional electric field like gate voltage, which promotes carrier transport and extraction in PDs.[38] Furthermore, time-resolved photoluminescence spectra (TRPL, excited from the front side) were employed to verify the promotion of carrier transport properties in these perovskite thin films (fitting parameters in Table S3 and S4). By analyzing PL emission at 750 nm, as shown in Figure 4e, we found that the carrier decay lifetime of G-PVK film (142 ns) is prolonged compared to that of C-PVK film (95 ns). Besides, with the aid of a top PCBM layer and a sub-PEDOT layer, the electron/hole diffusion length of G-PVK film and C-PVK film were also estimated (Figure S10) according to a 1D carrier diffusion model:[39]

$$L_D \approx \frac{2d\sqrt{2\left(\frac{\tau}{\tau_{hetero}}-1\right)}}{\pi} \quad (3)$$

where $\tau$ is the PL lifetime of the bare film, $\tau_{hetero}$ is the PL lifetime of the charge-transport layer/perovskite film, $d$ is the thickness of the perovskite film (the thicknesses

of C-PVK and G-PVK film are measured to be 300 nm and 890 nm, respectively). From C-PVK film, the electron and hole diffusion lengths are calculated to be 484 nm and 122 nm, respectively, while the electron and hole diffusion lengths are prolonged to be 893 and 291 nm in G-PVK film (Figure 4f). The improved carrier transport properties in a vertical gradient structure within the G-PVK film benefit the performance consistent with the PD device results.

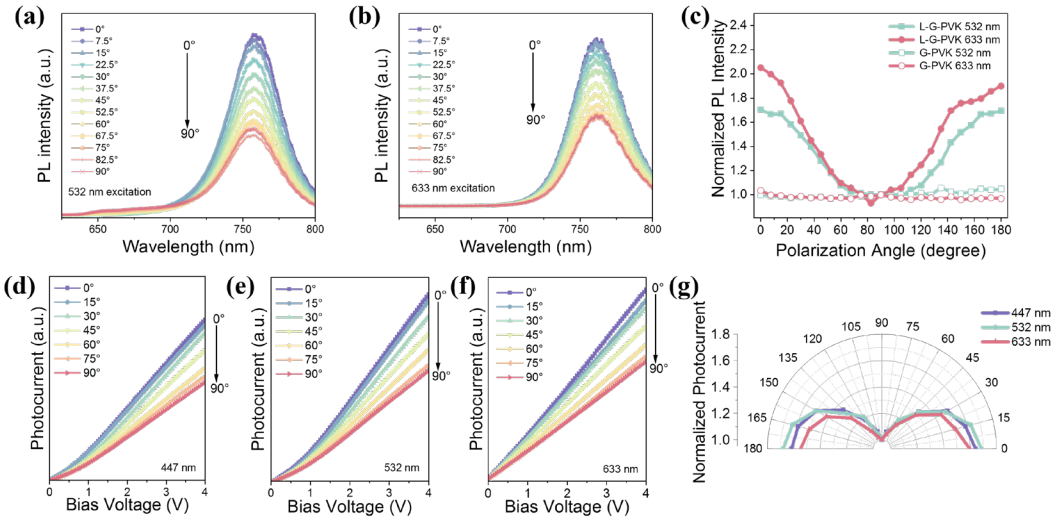


**Figure 5.** PL spectra of the L-G-PVK film with polarization angles from 0° to 90° relative to nanograting lines under a) 532 nm and b) 633 nm linearly polarized exciting sources. c) PL intensity at 750 nm as a function of polarization angle. *I-V* curves under polarized illuminations with wavelengths of d) 447, e) 532 and f) 633 nm with polarization angle from 0° to 90°. g) Photocurrent dependence from 0° to 180° polarization angle.

Besides promoting optoelectronic performances, another advantage of the linear nanopattern is endowing the device with the ability to detect polarization-sensitive light.[21-22, 40] This property was explained by the dielectric contrast between linear

structure (or NWs) and the surrounding environment and the resulting polarization-dependent optical absorbance.[29] We measured the PL of L-G-PVK film at room temperature with 532 nm and 633 nm linearly polarized laser, respectively. The polarization angle was defined as 0° when the polarization direction is parallel to the nanograting lines and 90° when the polarization direction is perpendicular to the nanograting lines. When the polarization angle changed from 0° to 90°, as shown in **Figure 5a** (532 nm excitation) and Figure 5b (633 nm excitation), the intensity of the PL peak declined. When the polarization angle was further changed from 90° to 180°, the PL peak intensity rose, as shown in Figures S12a and S12b. Figure 5c exhibits PL intensities at 757 nm (532 nm excitation) and PL intensities at 761 nm (633 nm excitation) as a function of the polarization angle. The trends of PL intensity for the L-G-PVK film are presented, and the polarization ratios (the PL intensity ratio between 0° and 90°) are calculated to be 2.05 for 532 nm excitation and 1.70 for 633 nm excitation. However, for G-PVK, the PL intensity did not change under the same operation (Figure S12c, S12d, and 5c). Furthermore, we measured the polarization dependence of the photocurrent of L-G-PD, as shown in Figure 5d-5f and Figure S12e-10g. The polarized lights were produced by LED illuminations with the 447, 532 and 633 nm wavelength penetrating a linear polarizer, as shown in Figure S11. The photocurrent of the L-G-PD device decreases with the polarization angle gradually declining from 0° to 90°. The polar plots of photocurrents with 4 V bias are shown in Figure 5g. The value of photocurrents with 4 V bias rose and fell when the polarization

angle changed from 0° to 180°. The peak-to-valley ratio of photocurrent calculated from polarization angles of 0° and 90° were estimated to be 1.64, 1.68, and 1.60 for 447, 532, and 633 nm illumination, respectively, which demonstrates a high polarization sensitivity of L-G-PD. Time-resolved photoresponse measurements were performed under 4 V bias with 447, 532, and 633 nm illumination, as shown in Figure S13. The polarization angle was gradually changed from 0° to 180° (with every time the illumination switched on and off, the polarizer was rotated 15°). It was shown that the photocurrent first decayed and then rose in this process. Performance parameters of our L-G-PD and several other reported perovskite polarization-sensitive photodetectors are compared in Table S5. The responsivity, detectivity, response time, and anisotropy ratio are higher than most previously reported perovskite polarization-sensitive photodetectors.

## 3. Conclusion

In summary, a polarization-sensitive perovskite photodetector (PSPPD) based on quasi-2D perovskite thin film was achieved with a polarization sensitivity of 1.68, responsivity of 89.8 A/W and detectivity of $1.5\times10^{12}$ Jones. The polarization detection based on a nanoimprinted linear pattern is available in a broadband range. Meanwhile, the linear pattern on the surface enhances the ability to harvest light, thereby improving the photodetector performance. Transient absorption (TA) and photoluminescence spectra demonstrated the spatial separation of 2D and 3D-like phases caused by hot-

casting. The charge carrier dynamics studied from TA spectra reveal the efficient charge funneling from small-n phases gathered at the bottom of the film to the top high-n phases, forming a photogating structure. This behavior of the charge carrier results in a long carrier lifetime and leads to the high responsivity of the photodetector. Our trial confirmed the feasibility of fabricating PSPPD on quasi-2D perovskite thin film. The research should facilitate the development of high-performance polarization-sensitive photodetectors.

## 4. Experimental section

*Materials:* MAI (>99.5%), PEAI (>99.5%), $PbI_2$ (lead iodide, >99.5%), PEDOT and PCBM (>99.5%) were purchased from Polymer Light Technology Corp. without further purification. DMF and DMSO were purchased from Sigma-Aldrich.

*Materials Synthesis:* PEAI, MAI and $PbI_2$ were dissolved at a stoichiometric ratio of 2:2:3 (following the ratio of $(PEA)_2(MA)_2Pb_3I_{10}$) in a DMSO/DMF (1:14 volume ratio) mixture, where the total $Pb^{2+}$ molar concentration is 0.5 M. The precursor solutions were then magnetically stirred at 70 °C for 4 hours.

*Device Fabrication:* The $Si/SiO_2$ (500 nm thickness for $SiO_2$) and glass substrates were ultrasonically cleaned sequentially in acetone, isopropyl alcohol, and DI water and then dried with nitrogen gas. Cr (10 nm)/Au (80 nm) electrodes with a channel width and

length of 500 and 4 μm were patterned via photolithography and E-beam deposition on the $Si/SiO_2$ substrates. The substrates were exposed to $O_2$ plasma for 10 min and preheated at 100 °C for 5 min with a PTFE spin-coating chuck. Then, 60 μL of precursor solution (70 °C preheating for 10 min before use) was dropped onto the preheated substrate, followed by a one-step spin-coating process at 3500 r.p.m. for 40 s. After spin-coating, the film was annealed at 110 °C for 10 min. Nanoimprinting was operated at the same time as annealing. The imprinting master was acquired from commercial DVD-R optical disks. The imprinting pressure was controlled by placing different numbers of metal blocks with a mass of 1.5 kg on the top of the template. With four metal blocks (6 kg in total), a suitable pressure for nanoimprinting can be obtained, and the pressure was calculated to be about 0.26 MPa. If the imprinting pressure is too low, the outlines of linear patterns copied onto the film surface will not be clear enough, as an example (with an imprinting pressure of 0.20 MPa) shown in Figure S14a. If the imprinting pressure is too high, the linear pattern on the film surface might be dilapidated, as an example (with an imprinting pressure of 0.39 MPa) shown in Figure S14b.

*Materials Characterization:* The surface morphology of films was measured by an atomic force microscope (Asylum MFP-3D Infinity). An X-ray Diffractometer (Rigaku SmartLab 9kW) was employed to measure X-ray diffraction spectra. Absorption spectra were measured with a UV-Vis-NIR spectrometer (Perkin Elmer). Grazing-

incidence wide-angle X-ray scattering (GIWAXS) was measured at the Shanghai Synchrotron Radiation Facility (SSRF), Shanghai, China. The incident angle is 0.1°, and the X-ray energy is 15 keV.

*Optical Measurements:* For femtosecond optical spectroscopy, the laser source was a Coherent LIBRA regenerative amplifier (150 fs, 1 kHz, 800 nm) seeded by a Coherent Vitesse oscillator (100 fs, 80 MHz). 800 nm wavelength laser pulses were from the regenerative amplifier's output, while 400 nm laser pulses were obtained with a BBO doubling crystal. The emission from the samples was collected at a backscattering angle of 150° by a pair of lenses and into an optical fiber that is coupled to a spectrometer (Acton, Spectra Pro 2500i) to be detected by a charge-coupled device (Princeton Instruments, Pixis 400B). TRPL was collected using an Optronis Optoscope streak camera system with an ultimate temporal resolution of 6 ps. Transient absorption measurements were performed using a Helios setup. The transient dynamics in fs-ns time region (50 fs - 7 ns) was acquired by Helios that works in a nondegenerate pump–probe configuration. The pump pulses were generated from an optical parametric amplifier (OPerA Solo) pumped by a 1-kHz regenerative amplifier (Coherent Libra, 800 nm, 50 fs, 4 mJ). A mode lock Ti-sapphire oscillator (Coherent Vitesse, 100 fs, 80MHz) was used to seed the amplifier. The probe pulse was a white light continuum generated by passing the 800 nm fs pulses through a 2 mm sapphire plate for the visible

part (420-780 nm). Measurements were carried out in a vacuum chamber to reduce any tendency for photo-oxidation.

*Optoelectronic Measurements:* The photoresponse performance under different wavelength lights were recorded by a four-probe station (LakeShore CRX-6.5K equipped with Keithley 4200 Semiconductor Characterization System) in ambient condition. The illumination sources were CW fiber lasers with wavelengths of 375 nm, 447 nm, 532 nm, 633 nm, and 750 nm. In polarized-light detection, the LEDs with 447 nm, 532 nm, and 633 nm were used as light sources.

## Supporting Information

Supporting Information is available from the Wiley Online Library or from the author.


## Acknowledgements

This work was financially supported by the Hong Kong Polytechnic University grant (1-CD7U).


## Conflict of Interest

The authors declare no conflict of interest.

References


[1] D. S. Smith, S. A. Eremin, *Anal. Bioanal. Chem.* **2008**, 391, 1499.

[2] J. Breckinridge, B. Oppenheimer, *Astrophys. J. Lett.* **2003**, 600, 1091.

[3] K. Yin, T. Zhan, J. Xiong, Z. He, S.-T. Wu, *Crystals* **2020**, 10, 561.

[4] J. S. Tyo, D. L. Goldstein, D. B. Chenault, J. A. Shaw, *Appl. Opt.* **2006**, 45, 5453.
[5] N. J. Jeon, J. H. Noh, Y. C. Kim, W. S. Yang, S. Ryu, S. I. Seok, *Nat. Mater.* **2014**, 13, 897.
[6] G. Xing, N. Mathews, S. Sun, S. S. Lim, Y. M. Lam, M. Grätzel, S. Mhaisalkar, T. C. Sum, *Science* **2013**, 342, 344.
[7] Y. Chen, J. Yin, Q. Wei, C. Wang, X. Wang, H. Ren, S. F. Yu, O. M. Bakr, O. F. Mohammed, M. Li, *Nat. Photonics* **2022**, 16, 485.
[8] L. Zhuang, Q. Wei, C. Li, H. Ren, Y. Li, F. Shi, L. Zhai, K. Leng, M. Li, S. P. Lau, *Adv. Opt. Mater.* **2022**, 10, 2201180.
[9] Y. Chen, C. Gao, T. Yang, W. Li, H. Xu, Z. Sun, *Chin. J. Struct. Chem.* **2022**, 41, 2204001.
[10] Q. Yao, K. Wang, J. Zhang, C. Li, C. Shang, F. Chen, Q. Huang, Q. Zhao, W. Zhang, X. Zhan, *Chin. J. Struct. Chem.* **2022**, 41, 2205077.
[11] T. Yang, Y. Li, S. Han, Z. Xu, Y. Liu, X. Zhang, X. Liu, B. Teng, J. Luo, Z. Sun, *Small* **2020**, 16, e1907020.
[12] C. Fang, M. Xu, J. Ma, J. Wang, L. Jin, M. Xu, D. Li, *Nano Lett.* **2020**, 20, 2339.
[13] L. H. Zeng, Q. M. Chen, Z. X. Zhang, D. Wu, H. Yuan, Y. Y. Li, W. Qarony, S. P. Lau, L. B. Luo, Y. H. Tsang, *Adv. Sci.* **2019**, 6, 1901134.
[14] L. Lu, W. Weng, Y. Ma, Y. Liu, S. Han, X. Liu, H. Xu, W. Lin, Z. Sun, J. Luo, *Angew. Chem., Int. Ed.* **2022**, 61, e202205030.
[15] J. Feng, X. Yan, Y. Liu, H. Gao, Y. Wu, B. Su, L. Jiang, *Adv. Mater.* **2017**, 29, 1605993.
[16] S. Pan, H. Zou, A. C. Wang, Z. Wang, J. Yu, C. Lan, Q. Liu, Z. L. Wang, T. Lian, J. Peng, Z. Lin, *Angew. Chem., Int. Ed.* **2020**, 59, 14942.
[17] S. X. Li, G. P. Zhang, H. Xia, Y. S. Xu, C. Lv, H. B. Sun, *Nanoscale* **2019**, 11, 18272.
[18] L. Gao, K. Zeng, J. Guo, C. Ge, J. Du, Y. Zhao, C. Chen, H. Deng, Y. He, H. Song, G. Niu, J. Tang, *Nano Lett.* **2016**, 16, 7446.
[19] Y. Zhou, J. Luo, Y. Zhao, C. Ge, C. Wang, L. Gao, C. Zhang, M. Hu, G. Niu, J. Tang, *Adv. Opt. Mater.* **2018**, 6, 1800679.
[20] H. Y. Hou, S. Tian, H. R. Ge, J. D. Chen, Y. Q. Li, J. X. Tang, *Adv. Funct. Mater.* **2022**, 32, 2209324.
[21] Y. Zhan, Y. Wang, Q. Cheng, C. Li, K. Li, H. Li, J. Peng, B. Lu, Y. Wang, Y. Song, L. Jiang, M. Li, *Angew. Chem., Int. Ed.* **2019**, 58, 16456.
[22] Q. Song, Y. Wang, F. Vogelbacher, Y. Zhan, D. Zhu, Y. Lan, W. Fang, Z. Zhang, L. Jiang, Y. Song, M. Li, *Adv. Energy Mater.* **2021**, 11, 2100742.
[23] L. Min, W. Tian, F. Cao, J. Guo, L. Li, *Adv. Mater.* **2021**, 33, e2101714.
[24] J. Qiu, Y. Zheng, Y. Xia, L. Chao, Y. Chen, W. Huang, *Adv. Funct. Mater.* **2018**, 29, 1806831.
[25] J. M. Hoffman, J. Strzalka, N. C. Flanders, I. Hadar, S. A. Cuthriell, Q. Zhang, R. D. Schaller, W. R. Dichtel, L. X. Chen, M. G. Kanatzidis, *Adv. Mater.* **2020**, 32, e2002812.

[26] Y. Liang, Q. Shang, Q. Wei, L. Zhao, Z. Liu, J. Shi, Y. Zhong, J. Chen, Y. Gao, M. Li, X. Liu, G. Xing, Q. Zhang, *Adv. Mater.* **2019**, 31, e1903030.
[27] G. Xing, B. Wu, X. Wu, M. Li, B. Du, Q. Wei, J. Guo, E. K. L. Yeow, T. C. Sum, W. Huang, *Nat. Commun.* **2017**, 8, 14558.
[28] Z. Wang, Q. Wei, X. Liu, L. Liu, X. Tang, J. Guo, S. Ren, G. Xing, D. Zhao, Y. Zheng, *Adv. Funct. Mater.* **2020**, 31, 2008404.
[29] J. Wang, M. S. Gudiksen, X. Duan, Y. Cui, C. M. Lieber, *Science* **2001**, 293, 1455.
[30] Y. Wang, P. Wang, X. Zhou, C. Li, H. Li, X. Hu, F. Li, X. Liu, M. Li, Y. Song, *Adv. Energy Mater.* **2018**, 8, 1702960.
[31] F. Cao, W. Tian, M. Wang, H. Cao, L. Li, *Adv. Funct. Mater.* **2019**, 29.
[32] B. Li, X. Huang, X. Wu, Q. Zuo, Y. Cao, Q. Zhu, Y. Li, Y. Xu, G. Zheng, D. Chen, X. H. Zhu, F. Huang, H. Zhen, L. Hou, J. Qing, W. Cai, *Adv. Funct. Mater.* **2023**, 33, 2300216.
[33] Y. W. Hsiao, B. S. Cheng, H. C. Hsu, S. H. Wu, H. T. Wu, C. C. Leu, C. F. Shih, *Adv. Funct. Mater.* **2023**, 33, 2300169.
[34] H. L. Loi, J. Cao, X. Guo, C. K. Liu, N. Wang, J. Song, G. Tang, Y. Zhu, F. Yan, *Adv Sci (Weinh)* **2020**, 7, 2000776.
[35] J. Liu, J. Leng, K. Wu, J. Zhang, S. Jin, *J. Am. Chem. Soc.* **2017**, 139, 1432.
[36] L. Zeng, W. Han, X. Ren, X. Li, D. Wu, S. Liu, H. Wang, S. P. Lau, Y. H. Tsang, C. X. Shan, J. Jie, *Nano Lett* **2023**, 23, 8241.
[37] S. Wei, F. Wang, X. Zou, L. Wang, C. Liu, X. Liu, W. Hu, Z. Fan, J. C. Ho, L. Liao, *Adv Mater* **2020**, 32, e1907527.
[38] H. Fang, W. Hu, *Adv. Sci.* **2017**, 4, 1700323.
[39] Z. Wang, J. Gan, X. Liu, H. Shi, Q. Wei, Q. Zeng, L. Qiao, Y. Zheng, *J. Power Sources* **2020**, 454, 227913.
[40] J. Zhang, J. Zhao, Y. Zhou, Y. Wang, K. S. Blankenagel, X. Wang, M. Tabassum, L. Su, *Adv. Opt. Mater.* **2021**, 9, 2100524.
[41] S. Lim, M. Ha, Y. Lee, H. Ko, *Adv. Opt. Mater.* **2018**, 6, 1800615.
[42] C. Ji, D. Dey, Y. Peng, X. Liu, L. Li, J. Luo, *Angew. Chem., Int. Ed.* **2020**, 59, 18933.
[43] Y. Li, T. Yang, Z. Xu, X. Liu, X. Huang, S. Han, Y. Liu, M. Li, J. Luo, Z. Sun, *Angew. Chem., Int. Ed.* **2020**, 59, 3429.
[44] W. Zhang, M. Hong, J. Luo, *J. Am. Chem. Soc.* **2021**, 143, 16758.
[45] F. Yang, K. Li, M. Fan, W. Yao, L. Fu, C. Xiong, S. Jiang, D. Li, M. Xu, C. Chen, G. Zhang, J. Tang, *Adv. Opt. Mater.* **2022**, 11, 2201859.